Design and Evaluation of an Ultra-Low-Cost Admittance-Controlled Haptic Paddle

by

Bjarne Aelbers

5185890

23-06-2026

Supervisor: Dr. Ir. A.H.A. Stienen, Biomechatronics Department, TU Delft
Faculty of Mechanical, Maritime and Materials Engineering (ME)
Delft University of Technology

TU Delft Delft University of Technology

Design and Evaluation of an Ultra-Low-Cost Admittance-Controlled Haptic Paddle

Bjarne Aelbers
Faculty of Mechanical Engineering, Delft University of Technology, The Netherlands

***Abstract*—Stroke is a leading cause of long-term disability and frequently results in upper-limb motor impairments that reduce manual dexterity and quality of life. Robotic assessment systems have been developed to provide objective quantification of these impairments; however, their high cost limits accessibility, particularly in low- and middle-income countries where the majority of stroke cases occur. This thesis investigates the feasibility of implementing admittance control in an ultra-low-cost haptic device intended as a hand-module extension for robotic stroke assessment. A single-degree-of-freedom haptic paddle was developed using widely available components and a total hardware budget below €50. The device incorporates force and position sensing, a DC motor actuation system, and an Arduino-based control architecture. An admittance controller was implemented to render programmable virtual inertia, damping, and stiffness, while a PID position controller provided motion tracking. System performance was evaluated through step-response, frequency-response, and position-tracking experiments involving human interaction. The developed device successfully achieved stable admittance-controlled interaction and is capable of rendering a range of virtual dynamic environments. Experimental results demonstrated accurate position tracking, consistent rendering of virtual dynamics, and stable operation despite the sensing, bandwidth, and actuation limitations associated with low-cost hardware. The system is capable of reproducing meaningful changes in virtual inertia, damping, and stiffness while maintaining user controllability and interaction stability. These findings demonstrate that admittance control is feasible on an ultra-low-cost haptic platform. The proposed design provides a promising foundation for affordable rehabilitation and assessment technologies and supports the development of accessible robotic tools for objective evaluation of post-stroke motor impairments.**

***Index Terms*—Admittance Control, Rehabilitation Robotics, Haptic Devices, Human–Robot Interaction, Stroke Assessment**

I. Introduction

Each year, approximately 11.9 million people worldwide experience a stroke, making it one of the leading causes of death and long-term disability globally [1]. Beyond its clinical impact, stroke imposes a substantial societal burden, with global costs estimated at 912 billion USD in 2017 and projected to rise to 1.6 trillion USD by 2050 [1].

Stroke often results in a range of motor impairments, including paresis, abnormal synergies, co-contraction, spasticity, and altered viscoelastic tissue properties [2]. In addition, sensory impairments may occur, such as loss of touch, temperature, pain, and proprioception [3]. These impairments significantly affect quality of life, particularly by reducing manual dexterity of the affected arm, which limits the ability to perform daily tasks involving hand use [4].

To assess these impairments in clinical practice, several standardized evaluation methods are commonly used. Common assessment tools, such as the Modified Tardieu Scale, the Modified Ashworth Scale, and the Fugl–Meyer Assessment, have several limitations, including high inter-rater variability, limited validity, and a lack of detailed information due to their ordinal scoring systems [5]. As a result, these assessments may lack sensitivity to subtle changes in motor function and may fail to distinguish between underlying impairment mechanisms.

The implementation of objective measurement systems may enable the acquisition of more reliable, quantitative, and comparable data across patients and clinical settings [6].

Several robotic quantification methods have been introduced to enhance existing clinical assessment instruments for upper-limb motor impairment [7]–[12]. At the Biomechatronics Laboratory in Delft, ongoing research is conducted using the Shoulder–Elbow Perturbator (SEP). This device is designed to classify the four primary elbow impairments observed in patients after stroke and to differentiate impairment scores of patients from those of healthy controls [5]. The SEP employs an admittance controller, enabling switching between free movement and precise perturbation velocity profiles [13].

Despite its demonstrated value, the SEP has two key limitations that restrict its broader applicability. First, the system is expensive, with an approximate hardware cost of €20.000,-, which limits its accessibility in primary-care in low- and middle-income countries. Second, the SEP primarily focuses on shoulder and elbow dynamics, which limits its ability to capture multi-joint coordination patterns, such as pathological synergies involving the hand and wrist. As a result, the current configuration only partially characterizes the complex motor impairments observed after stroke.

Approximately 77% of stroke cases occur in low- and middle-income countries [1], where access to advanced rehabilitation technologies is often limited by financial constraints. Consequently, the development of cost-effective systems is essential to improve accessibility and scalability of rehabilitation technologies. In addition to enhancing the understanding of motor impairments, such systems could be integrated into rehabilitation programs to reduce the physical burden on clinicians and potentially lower overall healthcare costs [14].

Further optimization of the system is therefore required to enable robust assessment of these synergies. In line with ongoing efforts to make the SEP more cost-effective and thus more widely accessible, additional developments are being

pursued to expand its measurement capabilities. At present, the SEP lacks a dedicated hand module, which limits its ability to capture the multi-joint interactions that contribute to pathological synergies. To address these limitations, this thesis investigates the feasibility of implementing admittance control in an ultra-low-cost haptic device designed to extend the SEP with a hand module.

Replacing high-end components with low-cost alternatives introduces several technical challenges, including increased time delay, higher measurement noise, reduced sensor accuracy, drift in force measurements, and limited encoder resolution. These factors can degrade system dynamics and compromise the stability and reliability of human–robot interaction. Therefore, it is essential to evaluate their impact on control performance. In addition to cost, component availability is a key consideration, as the system should be reproducible using widely accessible parts.

To ensure safe and effective interaction with the user, the device must render controlled mechanical environments while remaining compliant. Admittance control is adopted for the hand module, as it enables compliant and stable interaction while allowing controlled perturbations to be applied. This makes it well suited for safe human–robot interaction and for provoking neuromechanical responses required to characterize motor impairments.

To determine whether the low-cost system can deliver stable human–robot interaction and render meaningful dynamics, standardized interaction tasks are required. Such tasks are widely used to evaluate haptic devices and human motor control. Two relevant examples are pick-and-lift tasks and position-tracking tasks, which together probe force regulation, motion control, and coordination. Pick-and-lift tasks assess how users modulate grip and load forces in different situations [15]–[17]. In these tasks, participants are asked to lift varying apparatus weighing up to 400 grams anywhere between 20 - 40 cm. Whereas position-tracking tasks evaluate accuracy and stability when following or maintaining a target trajectory under varying dynamic conditions [7], [18]. Because these tasks yield repeatable, quantitative metrics, they are well suited for assessing both human–robot interaction quality and controller performance.

These considerations motivate the exploration of low-cost alternatives to existing robotic systems. In particular, it is of interest to investigate whether advanced control strategies can be implemented on affordable hardware platforms.

This motivates the central research question of this thesis:

Is admittance control feasible in an ultra-low-cost haptic device?

Based on this objective, the development of a low-cost haptic device must satisfy the following requirements:

- The device shall be capable of exerting up to 4 N of interaction force.
- The device shall provide a minimum vertical motion range of 30 mm.
- The system shall support admittance control to render virtual dynamics.
- The total system cost shall not exceed 50 euros.
- Components shall be widely available to ensure reproducibility.
- The device shall be capable of simulating varying mass, damping, and stiffness.

II. Background

A. Shoulder Elbow Perturbator

The SEP is designed to apply controlled perturbations to the elbow joint in the horizontal plane while providing adjustable shoulder support. During operation, the elbow joint of the participant is aligned with the rotational axis of the device, and the forearm is fixed near the wrist to ensure an accurate transmission of motion and torque between the participant and the system. The SEP can seamlessly switch between admittance and velocity control modes, enabling both compliant interaction and precisely controlled movements required for stroke-related motor assessments.

The SEP implements admittance control to realize programmable virtual dynamics during human–robot interaction. The controller utilizes the measured interaction torque, elbow angle, and angular velocity as input variables. Based on these measurements and predefined virtual parameters, including disturbance torque, virtual mass, stiffness, and damping, the system computes the desired angular acceleration. The computed acceleration is subsequently integrated to obtain the desired angular velocity, which serves as the reference input for the velocity controller. This enables the SEP to reproduce configurable dynamic behaviors and controlled perturbations during elbow movement experiments.

The SEP uses the desired angular velocity as the input to the velocity controller, independent of external loading from the combined dynamics of the participant's arm and the device. A velocity servo controller is tuned to track this reference by generating the required motor torque. Angular position and velocity are continuously measured by an encoder for both control and post-processing analysis.

B. Admittance vs Impedance

Both admittance control and impedance control offer distinct advantages and limitations. Impedance control simulates compliant interaction effectively but struggles to render high stiffness. It relies on low-inertia, highly backdrivable actuators for accurate force reproduction [19], [20]. Admittance control can render high stiffness but is less suited for compliant interaction and is sensitive to sensor noise, delays, and force-measurement errors [19], [20]. However, with appropriate hardware and controller design, admittance control can achieve fine compliant behavior, making it well suited for precise perturbations.

In the context of post-stroke rehabilitation, the investigation of motor synergies requires accurate measurement of fine

Fig. 1: *Overview of the Shoulder Elbow Perturbator (SEP). The participant's forearm is attached to the lever arm, while the elbow joint is aligned with the motor rotation axis to enable controlled perturbations. Source: https://hankamprehab.nl/de-schouder-elleboog-perturbator-sep/*

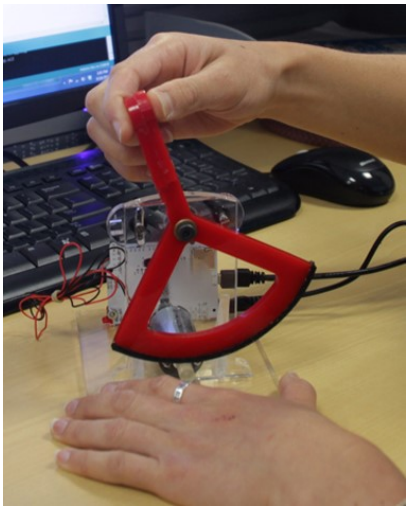

Fig. 2: *The first iteration of the Hapkit prototype. This version features a laser-cut structural frame, with a DC motor driving the handle through a friction-based wheel interface. A custom-designed PCB provides motor control and signal processing. Source: https://hapkit.stanford.edu/build.html*

and coordinated movements under varying conditions. This necessitates a controlled and compliant interaction environment that can respond sensitively to small user inputs. Such an environment is typically realized through a "soft" virtual dynamic, allowing safe and intuitive interaction between the user and the device.

Admittance control is particularly suitable for this purpose, as it enables the system to generate motion in response to user-applied forces. This allows the implementation of virtual dynamics—such as mass, damping, and stiffness—which can be tuned to study motor behavior under different conditions.

C. Hapkit

Building on the need for affordable extensions to existing rehabilitation devices, it is relevant to investigate whether a low-cost hand module can be developed without significantly compromising performance. Figure 2 shows a well-known example of an affordable haptic system called the Hapkit. It is a low-cost, open-source kinesthetic haptic device originally developed for educational purposes [21]. The hardware components required for the Hapkit typically range between 50 and 100 USD [22], making it an attractive platform for rapid prototyping and research. The system is typically implemented using impedance control, where a prescribed motion results in the generation of an interaction force [21].

More advanced implementations have extended the capabilities of such systems. For example, ETH Zurich developed an admittance-controlled variant incorporating a Maxon brushed DC motor (type RE 25339156), a custom linear current amplifier, a piezoresistive force sensor, and a regulated laboratory power supply [23]. While these components improve performance, they significantly increase system cost. Notably, the motor alone costs approximately 270 euros, highlighting the trade-off between performance and affordability.

III. Method

A. Mechanical Design

The developed hand module is based on the Hapkit platform [21]. In contrast to the original Hapkit design, which is oriented vertically, the proposed hand module is rotated by 90 degrees to enable vertical movement of the handle. Additionally, a force sensor is integrated between the grip interface and the main axle to enable admittance control. A representation of the hand module is shown in Figure 3. The device provides a single degree of freedom, and during operation the participant interacts with the distal end of the handle using a pinch grip. The module allows controlled upward and downward movements to facilitate the evaluation of precise motor control during tracking tasks.

As shown in Figure 4a, the capstan is mounted directly onto the DC motor shaft, while the DC motor itself is fixed to the drive mount. The angle encoder is also attached to the drive mount and aligned coaxially with the capstan, additionally a magnet is placed at the end of the capstan as shown in 4b. The capstan is actuated by the DC motor and connected to the handle drum via a nylon fishing line. The line is wrapped five times around the capstan. With each additional wrap, the effective friction coefficient increases exponentially, resulting in a transmission with negligible backlash. An additional advantage of this configuration is its low operational noise.

Both ends of the nylon line are secured to the sides of the handle drum using serrated flange nuts and bolts. The drive mount can be adjusted to minimize the distance between the capstan and the handle drum, thereby optimizing the transmission geometry. The handle drum and the distal tip of the handle are mechanically connected through a load cell, enabling force measurement. The entire handle assembly rotates about an axle aligned with the DC motor shaft. Mechanical end stops are

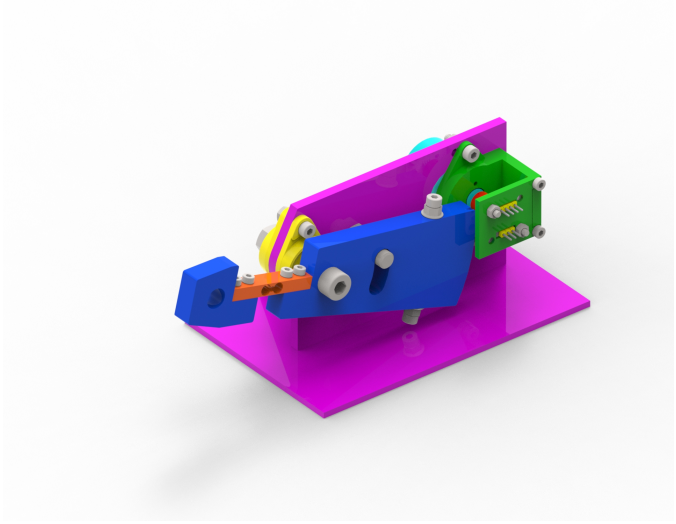

Fig. 3: *Redesigned Hapkit system with color-coded components: base (purple), handle (blue), bearings (yellow), DC motor (cyan), Encoder & motor bracket (green), capstan (red), and load cell (orange).*

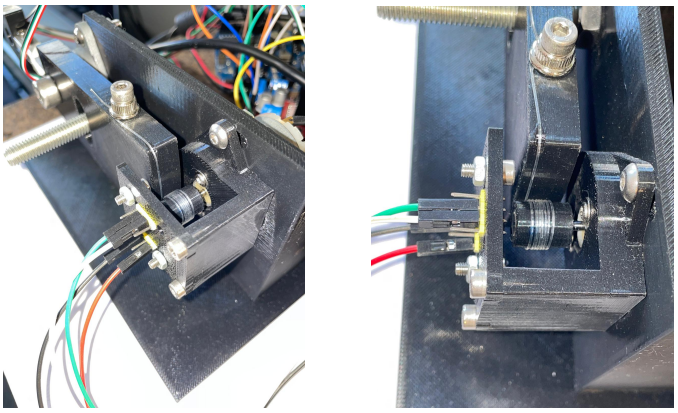

(a) *Capstan drive*

(b) *Close up capstan drive and magnet*

Fig. 4: *The capstan drive for the hand module.*

implemented by inserting a bolt into the center of the drum. A slot in the drum constrains the handle rotation.

The capstan must provide sufficient space to accommodate the diametrically magnetized magnet supplied with the encoder. This magnet has a diameter of 5 mm. To allow for proper installation and removal during assembly and maintenance, a minimum capstan diameter of 10 mm is required. Therefore, the capstan radius was set to $r_c = 5$ mm.

A micro load cell with a rated capacity of 0.78 kg was selected as the smallest and most cost-effective option for measuring forces up to 4 N. Its 45.2 mm body length, combined with a 10 mm integration allowance on each side, resulted in a required handle radius of $r_h = 65$ mm.

The drum radius was selected to ensure full use of the 7.65 N measurement range of the micro load cell. Solving equation 7 for r_d using the parameters defined above yields a drum radius of $r_d = 82.4$ mm.

To achieve a vertical displacement of 30 mm, the required rotation angle α is calculated using equation 1, resulting in an operating range of $\alpha = 26.7°$.

$$\alpha = \arctan\left(\frac{h}{2r_h}\right) \tag{1}$$

To ensure that the capstan motion remains within the physical limits of the drum, a safety margin of $\beta = 3.2°$ was applied on both sides. The corresponding derivation is provided in Appendix VII-A. Including this margin yields a total drum angle of $\gamma = 33.2°$.

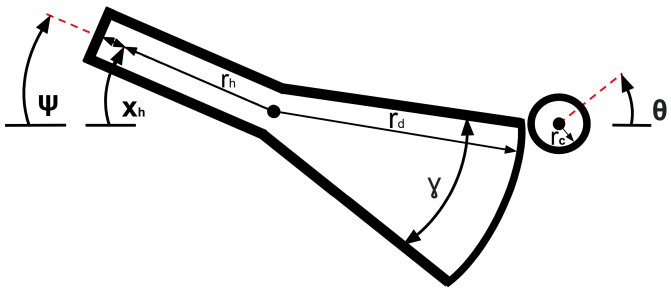

Fig. 5: *Kinematic diagram of the hand module. The module is modeled as two rigid bodies rotating in contact without slipping. Here, x_h represents the handle position, r_h the radius of the handle, r_d the radius of the drum, r_c the radius of the capstan, θ the capstan angle, and ψ the handle angle.*

Figure 5 shows that the Hapkit is modeled as two rigid bodies: the paddle and the capstan. These bodies roll in contact with each other, and it is assumed that no slipping occurs between them. Since the motion of the system is driven by the capstan and its angle is measured, the handle displacement x_h can be expressed as a function of the capstan angle θ.

$$x_h = r_h\psi \tag{2}$$

$$r_c\theta = r_d\psi \tag{3}$$

Combining these expressions yields

$$x_h = \frac{r_c r_h}{r_d}\theta \tag{4}$$

When analyzing the free-body diagram shown in Figure 6, the relationship between the force exerted on the handle and the torque applied by the DC motor can be derived. The force that is applied by the user F_{lift}, can be determined into F_{lifty} by vector addition. By substituting τ_ψ from Equation 5 into Equation 6, the relationship between the handle force F_{lifty} and the motor torque is obtained, as shown in Equation 7.

$$F_d = \frac{\tau_\theta}{r_c} = \frac{\tau_\psi}{r_d} \tag{5}$$

$$F_{lifty} = \frac{\tau_\psi}{r_h} \tag{6}$$

$$F_{lifty} = \frac{r_d}{r_h r_c}\tau_\theta \tag{7}$$

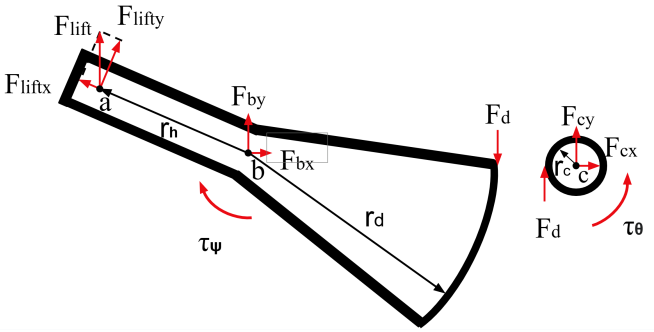

Fig. 6: *The free body diagram of the hand module. The diagram specifies the force components at points a, b, and c. The lift force of the user F_{lift} and the decoupled components F_{liftx}, F_{lifty}. The drum force F_d. The reaction forces in point b F_{bx}, F_{by}. The reaction froces in point c F_{cx}, F_{cy}. The position vectors r_h, r_d, and r_c denote the corresponding moment arms used to compute the torques τ_ψ and τ_θ.*

With the parameters defined above, the hand module achieves a vertical travel of 30 mm and a maximum output force of 7.65 N, where $r_c = 5$ mm, $r_d = 82.4$ mm, and $r_h = 65$ mm.

B. Hardware

The control platform is implemented on an Arduino Uno R3 operating at 16 MHz, with USB serial communication used for external interfacing and data logging. This microcontroller is theoretically capable of sustaining interrupt frequencies in the order of several tens of kHz under minimal computational load, practical performance is constrained by processing overhead and serial communication latency, which can introduce delays on the order of milliseconds depending on baud rate and data throughput. These effects contribute to phase lag and timing jitter within the control loop, which can negatively affect the stability and transparency of the admittance controller, particularly in high-stiffness or low-damping virtual environments.

The actuation system consists of a 12 V DC motor driven by an L298N H-bridge driver. The L298N introduces a significant voltage drop of approximately 1.5 V–2.5 V due to its bipolar transistor structure, reducing effective torque output and linearity. The PWM switching frequency is typically in the range of 1–20 kHz; however, motor response is dominated by mechanical dynamics rather than electrical switching. The DC motor itself exhibits cogging and dead zone. Since cogging torque and low-speed nonlinearities are typically not specified for low-cost brushed DC motors, actuator selection was based on experimental evaluation rather than datasheet comparison. Multiple locally available motors were qualitatively assessed for rotational smoothness and perceived cogging behavior, resulting in the selection of the Velleman MOT3N. Although the Hapkit platform recommends the Mabuchi RF-370CA-15370 motor for haptic applications, this actuator was not locally available within the required project timeline.

Position feedback is provided by an AS5600 magnetic rotary encoder with a nominal 12-bit resolution, corresponding to an angular step size of approximately 0.087°. Although this is a high angular resolution, practical accuracy is reduced by magnetic alignment tolerances and mounting conditions. The sensor communicates via I2C with clock rates up to 1 MHz; however, the effective update frequency is typically limited to approximately 500–1000 Hz, depending on bus load and polling strategy. This introduces discretization noise and minor delay in velocity estimation, particularly at low-speed motion.

The force measurement consists of a 0.78 kg strain gauge load cell combined with an HX711 24-bit amplifier. The load cell exhibits typical nonlinearity ±0.05% FS, hysteresis ±0.05% FS, non-repeatability ±0.05% FS, and creep 0.1% FS/30 min, corresponding to sub-gram level deviations in practice. In addition, thermal sensitivity on the order of 0.05% FS/10°C introduces slow-varying drift in the force baseline [24]. The HX711 further has its fixed output data rates of 10 Hz and 80 Hz, where the higher sampling mode increases measurement noise to the order of several least significant counts, reducing force signal smoothness at higher bandwidths. As a result, the effective force measurement bandwidth remains below 80 Hz, with observable low-frequency drift and quantization noise. To achieve 80 Hz, some modifications are required to the HX711 amplifier. It is necessary to disconnect pin 15 from the PCB and connect it directly to pin 16.

Overall, the combined system exhibits a deviation in sensing, actuation, and control bandwidths: force sensing is limited to 80 Hz, position sensing operates up to approximately 1 kHz, and control execution is constrained to a few kilohertz. An overview of the hardware, timing, and costs can be found in Table I.

C. Software

The control system for this module is implemented using a combination of Arduino-based embedded control and Python-based data processing and real-time interface.

1) Arduino: The Arduino firmware is structured around a real-time interrupt-driven architecture. A hardware timer (Timer2) triggers the control loop at 1 kHz, in which the following steps are executed:

- Computation of the admittance reference signal.
- Execution of the PID controller.
- Motor actuation via PWM and direction pins.

Sensor acquisition is handled in the main loop at lower rates, where the encoder is set to sample at 1 kHz and the load cell at 100 Hz. The encoder signal is processed to obtain a continuous angle, and numerical differentiation is used to estimate angular velocity and acceleration.

The admittance controller is implemented as a discrete-time second-order system, where the input torque is computed from the measured force. The system states are updated using semi-implicit Euler integration. A clamping strategy is applied to the admittance dynamics to prevent wind-up behavior.

The PID controller comprises proportional, integral, and derivative terms, with optional filtering applied to the deriva-

TABLE I: *Overview of components and corresponding hardware used in the hand module.*

Component	Hardware (Model / Brand)	Frequency / Timing	Cost (€)
Microcontroller	Arduino UNO v3	10.000 Hz	9.50
Motor Driver	L298N Motor Driver Module	N/A	5.00
Angle Encoder	AS5600 Magnetic Encoder	1000 Hz	3.00
Load Cell	0.78 kg Micro Load Cell	N/A	5.00
Load Cell Amplifier	HX711	10 Hz / 80 Hz	2.00
DC Motor	Velleman MOT3N DC Motor	N/A	2.00
Bearings	KFL8 bearing axle-mount	N/A	5.00
Wiring	Jumper cable set	N/A	1.50
Bolts and nuts	Assorted fasteners	N/A	3.00
Power Supply	12 V 3 A adapter	N/A	5.00

tive action. A conditional anti-windup mechanism is included to prevent integrator saturation.

To facilitate analysis, all relevant variables (angle, target, PWM, velocity, acceleration, and PID terms) are packed into a binary log structure and set to be transmitted at 250 Hz.

During the admittance tasks, the main loop, encoder, force sensor, and logger operate at sampling rates of 1000 Hz, 726 Hz, 76 Hz, and 222 Hz, respectively.

2) Python: The Python software is structured around real-time data acquisition, visualization, and offline post-processing. Serial communication is established with the Arduino-based controller at 250000 bps, where binary data packets are continuously received, decoded, and stored for analysis.

A graphical user interface (GUI) is implemented using the `tkinter` library to provide real-time task instructions and visual feedback to the participant. A state-machine architecture is used to control the different experimental phases, including hold and movement tasks, while simultaneously updating the live visualization and logging data.

Offline processing and visualization were performed using NumPy, SciPy, and Matplotlib. Depending on the experimental mode, the analysis included frequency-response estimation, filtering, coherence analysis, force reconstruction, and step-response characterization. Performance metrics such as gain and phase margins, cutoff frequency, rise time, settling time, overshoot, and root-mean-square error (RMSE) were calculated to evaluate system behavior and controller performance.

D. Control Scheme

The hand module is controlled using an admittance control strategy. This consists of a position control loop combined with a virtual dynamics model. Together, these components form the admittance controller, where interaction forces are translated into desired motion, which is subsequently tracked by the position controller.

1) Admittance Control: The admittance controller, shown in Figure 7, takes the external torque as its input, which is derived from the geometric relationship between the handle and the force measured by the micro load cell. Based on the selected virtual inertia, damping, and stiffness parameters, the controller imposes a set of virtual dynamics that define the system response in terms of angular acceleration, velocity, and position.

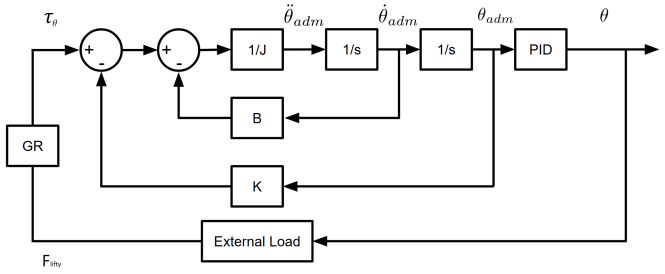

Fig. 7: *Block diagram of the admittance control architecture. The measured external force F_{lifty} is converted into an interaction torque τ_θ through the geometric relation (GR). This torque is used to compute the virtual dynamics defined by the inertia J, damping B, and stiffness K parameters. The resulting admittance acceleration $\ddot{\theta}_{adm}$ is integrated twice to obtain the desired admittance velocity $\dot{\theta}_{adm}$ and position θ_{adm}. This desired position serves as the reference input for the PID position controller, which drives the system to produce the actual angle θ.*

The virtual dynamics are given in Equation 8, where the admittance acceleration is computed from the applied torque and the selected virtual parameters. By integrating the resulting acceleration twice, the admittance angle is obtained, which represents the desired reference motion of the system. This reference is subsequently provided to the PID position controller.

$$\ddot{\theta}_{adm} = \frac{\tau_\theta - B_{adm}\dot{\theta}_{adm} - K_{adm}\theta_{adm}}{J_{adm}} \tag{8}$$

With admittance control, there is a possibility that the calculated admittance angle θ_{adm} exceeds the physical operating range of the mechanism. When this occurs, the system is driven against its mechanical limit and remains there until θ_{adm} returns to a value within the allowable range. This behavior can result in a sticky or sluggish sensation near the maximum and minimum angles of motion.

To mitigate this effect, a clamping mechanism is incorporated into the admittance control loop. The admittance state is constrained according to:

$$\left(\theta_{adm}, \dot{\theta}_{adm}\right) = \begin{cases} (\theta_{max}, 0), \text{if } \theta_{adm} > \theta_{max} \wedge \dot{\theta}_{adm} > 0 \\ (\theta_{min}, 0), \text{if } \theta_{adm} < \theta_{min} \wedge \dot{\theta}_{adm} < 0 \end{cases} \tag{9}$$

Under these conditions, the virtual dynamics are halted in the constrained direction, thereby preventing windup at the

motion boundaries. Normal admittance behavior resumes once the system motion reverses toward the admissible operating range. This strategy preserves controller responsiveness while ensuring compliance with the physical limits of the system.

2) Position Control: Position control is implemented using a PID controller, which is responsible for tracking a desired target angle. The controller continuously compares the target angle θ_{adm} with the measured angle θ to compute a control error. Based on this error, proportional, integral, and derivative actions are combined to generate the control signal. This signal determines how the actuator responds, so that the measured angle is driven toward the target value. The resulting control law can be expressed as

$$u(t) = K_p e(t) + K_i \int_0^t e(\tau)\, d\tau + K_d \frac{de(t)}{dt} \tag{10}$$

For analysis in the frequency domain, Equation 10 can be transformed using the Laplace transform. This results in the following transfer function representation of the PID controller:

$$\frac{U(s)}{E(s)} = K_p + \frac{K_i}{s} + K_d s \tag{11}$$

This representation is used to give a visual understanding on how the proportional, integral, and derivative terms operate. Figure 8 illustrates these components, including additional implementations addressing two practical issues: integrator windup and the amplification of measurement noise by the derivative term.

Integrator windup is mitigated using a conditional integration scheme with active unwinding. When the controller output saturates, the integral term is prevented from accumulating error unconditionally. Instead, integration is only performed if it drives the system out of saturation; otherwise, it is clamped. This prevents excessive integrator buildup during actuator limits [25].

An active unwinding mechanism is incorporated to improve recovery from accumulated integral error. Because a user may hold a fixed position and generate sustained error, rapid correction is required without relying on slow integral decay. When the integral term opposes the current error, it is driven toward zero at an accelerated rate. This approach improves controller responsiveness.

Another aspect that must be considered is the sensitivity of the derivative term to measurement noise. Since the derivative term is proportional to the rate of change of the control error, high-frequency noise in the measured signal can be amplified. To mitigate this effect, a first-order low-pass filter is applied to the error signal prior to computing the derivative term. This reduces the influence of noise while preserving the predictive behavior of the derivative action.

The actuator model accounts for both minimum and maximum PWM limits. In this system, motion starts at a bias of 139 PWM, while the maximum output is 255. To handle this nonlinearity, the controller output is passed through an inverse dead-zone before saturation, ensuring consistent behavior over the full operating range.

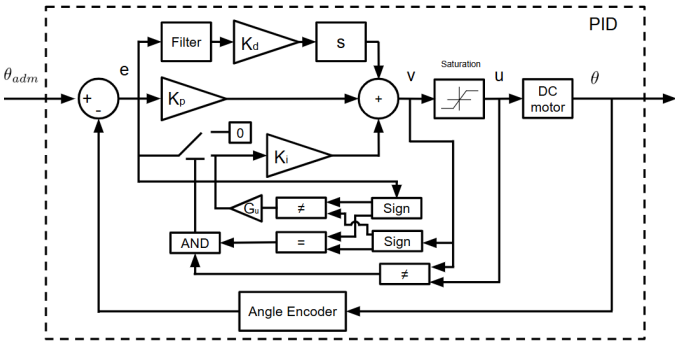

Fig. 8: *Block diagram of the PID position control system used to track the desired handle angle. The error between the desired and measured angle is processed by proportional (K_p), integral (K_i), and derivative (K_d) control actions. A low-pass filter is applied to the derivative term to reduce noise amplification, while a conditional integrationscheme with back-calculation prevents integrator windup when actuator saturation occurs. The resulting control signal drives the DC motor, and the actual angle is measured using an encoder to close the feedback loop.*

E. Controller Tuning

The tuning of the PID controller is performed using the Ziegler–Nichols method. This method utilizes the system response to determine suitable controller parameters. The first step in this procedure is to increase the proportional gain until the system reaches the point of sustained oscillations. This gain is referred to as the ultimate gain K_u. At this point, the period of oscillation is measured, which is known as the ultimate period T_u.

Using these parameters, the controller gains can be determined according to the Ziegler–Nichols tuning rules. In this case, both the proportional and integral terms are required. The integral term is used to eliminate steady-state error, while the derivative term provides additional damping to the system. Since the system is intended to be operated while in contact with a human hand, the user interaction can be considered as a source of additional damping. Nevertheless, both PI and PID controllers are evaluated using the following tuning rules:

$$\text{PI:} \quad \begin{cases} K_p = 0.45 K_u \\ K_i = 0.54 \frac{K_u}{T_u} \end{cases} \tag{12}$$

$$\text{PID:} \quad \begin{cases} K_p = 0.6 K_u \\ K_i = 1.2 \frac{K_u}{T_u} \\ K_d = 0.075 K_u T_u \end{cases} \tag{13}$$

The system is tuned while accounting for human interaction, with the user applying a loose pinch grip to the handle. A step input of 10° (from -5° to $+5^\circ$) is used, and the proportional gain is increased in increments of 0.1.

A chirp test is performed to assess stability of the controller. The chirp input spans 0.1–100 Hz with a 5° amplitude, and its excitation frequency follows a power-law distribution.

F. Admittance Evaluation

The admittance controller is evaluated using a position-tracking task. The experiment begins at $0°$, corresponding to the neutral handle position. Figure 9 shows the graphical user interface (GUI), which provides instructions and real-time feedback by displaying the range of motion on the horizontal bar, the target angle as a vertical bar, and the current handle angle as an oval marker. The participant follows three commands: *move up*, *move down*, and *hold position*.

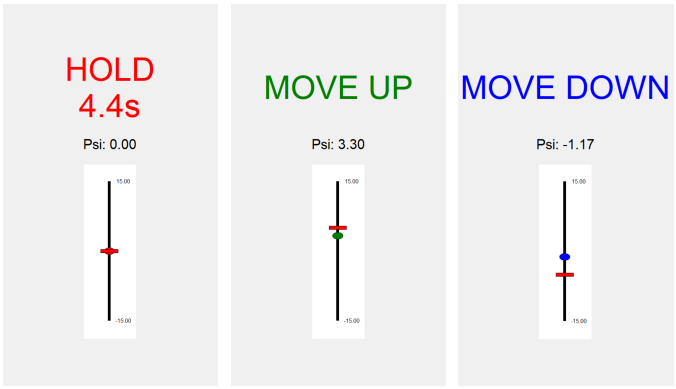

(a) *Turns red "hold position".* **(b)** *Turns green "move up".* **(c)** *Turns blue "move down".*

Fig. 9: *At the top of the interface, the available commands are displayed. Below them, the real-time measured angle is shown, and at the bottom, the tracking bar is presented. Three commands are available: hold position, move up, and move down. The tracking bar indicates the maximum and minimum angle at the top and bottom, respectively. The horizontal red bar represents the target angle, while the ellipsoidal marker shows the measured angle and changes color depending on the active command.*

The task consists of four phases:

1) Maintaining $0°$ for 5 s.
2) Moving to $+5°$ and holding for 5 s.
3) Moving to $-5°$ and holding for 5 s.
4) Returning to $+5°$ for a final 5 s hold.

Accurate rendering of virtual inertia is essential for admittance-controlled rehabilitation devices because impairment assessments rely on predictable and reproducible interaction dynamics. Therefore, the achievable virtual inertia range of the proposed low-cost device was investigated.

This is achieved by incrementally increasing the inertia and assessing stability until the system exhibits unstable behavior or reaches practical limits. Once this range is identified, three inertia values—minimum, maximum, and midpoint—are selected for further evaluation. Each task is repeated five times, and the resulting angle, angular velocity, angular acceleration, and moment are plotted. The kinematic variables are obtained from the virtual dynamics using the measured force as input to Equation 8, while the theoretical force is computed from the measured angle θ, which is differentiated to obtain angular velocity and acceleration. This enables cross-validation between measured and theoretical quantities. Additionally, angle error, moment error, and normalized moment error are summarized using box plots. The RMSE of the angle and task error is computed for each 5 s hold segment, and the moment RMSE is obtained by comparing the calculated and measured moments. The normalized moment RMSE is computed by dividing the 30 s measurement into multiple 2 s segments and averaging the absolute maximum force within each segment.

In addition to verifying correct operation of the virtual dynamics, the system stiffness and damping are also evaluated. Maximum damping and maximum stiffness are tested in combination with the medium inertia, and the resulting angle and moment responses are plotted to confirm expected behavior. Finally, the medium inertia combined with both maximum damping and maximum stiffness is assessed.

IV. Results

A. PI/PID Step Response

Before evaluating admittance control, the position controller must be tuned to ensure accurate tracking of the generated reference trajectory. Therefore, a step-response analysis was performed to determine suitable controller gains and assess closed-loop stability.

Figure 10 shows the system response at the ultimate gain $K_u = 4.5$. Sustained oscillations occur after the step input, indicating marginal stability. The reduction in oscillation amplitude before the step corresponds to the moment when the hand engages with the handle, introducing additional damping.

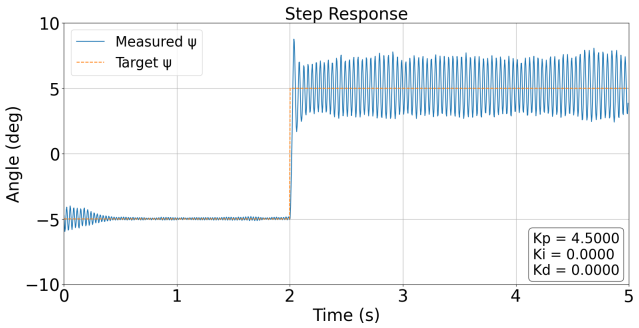

Fig. 10: *Step response of the system at the ultimate gain $K_u = 4.5$, showing sustained oscillations after the step input. The reduction in oscillations prior to the step indicates the moment at which the hand engages in a loose pinch grip, introducing additional damping.*

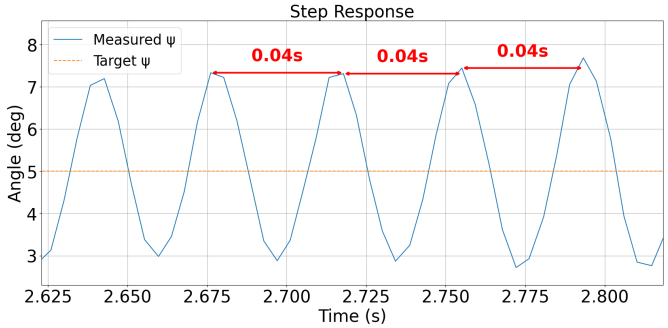

Fig. 11: *Zoomed-in view of the oscillations used to determine the ultimate period $T_u = 0.04$ s.*

A zoomed-in view of the oscillatory behavior is shown in Figure 11, where the oscillation period is measured as $T_u = 0.04\ s$.

Both the ultimate gain and the oscillatory period are inserted into Equation 12 to determine the PI controller gains, resulting in $K_p = 2.025$ and $K_i = 60.75$. The corresponding step response is shown in Figure 12. Sustained oscillations are observed after the step input, indicating marginal stability.

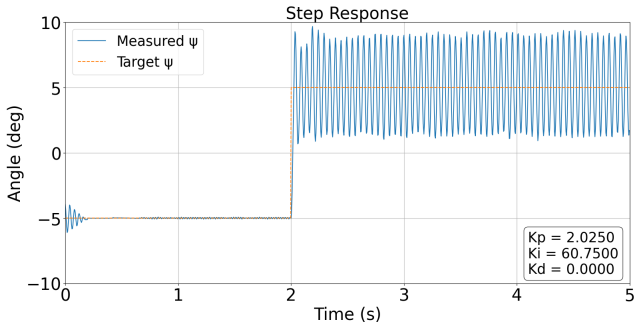

Fig. 12: *Step response of the system using PI control, showing sustained oscillations and limited damping. The reduction in oscillations prior to the step indicates the moment at which the hand engages with the system.*

To ensure that the underlying position controller forms a stable and responsive inner loop for subsequent admittance-control experiments, the PID controller was evaluated using the same tuning procedure. Substituting the measured ultimate gain and period into Equation 13 yields $K_p = 2.7$, $K_i = 135$, and $K_d = 0.0135$. The resulting step response is shown in Figure 13.

The system exhibits underdamped behavior, with a rise time of 0.021 s, an overshoot of 21.9%, and a settling time of 0.165 s. Compared to PI control, the inclusion of the derivative term reduces sustained oscillations and improves transient stability. These results indicate that the PID controller provides sufficient stability and responsiveness to serve as the inner control loop for the admittance-control experiments.

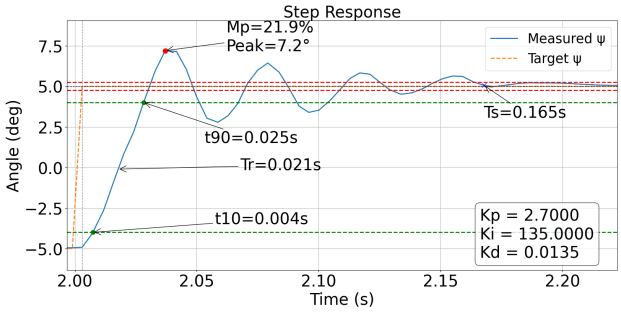

Fig. 13: *Step response of the system using PID control with human interaction. The response exhibits a rise time of* $0.021\ s$*, an overshoot of* 21.9%*, and a settling time of* $0.165\ s$*.*

B. PID Chirp Test

In addition to transient performance, admittance control requires sufficient bandwidth and robustness. Therefore, a chirp test was performed to characterize the frequency response of the closed-loop position controller, as shown in Figure 14. The response indicates second-order system behavior with a cutoff frequency of 33.3 Hz, a phase margin of $46.1°$, and a gain margin of 13.2 dB. The coherence remains above 0.9 up to 60 Hz. These margins indicate stable closed-loop behavior with moderate robustness.

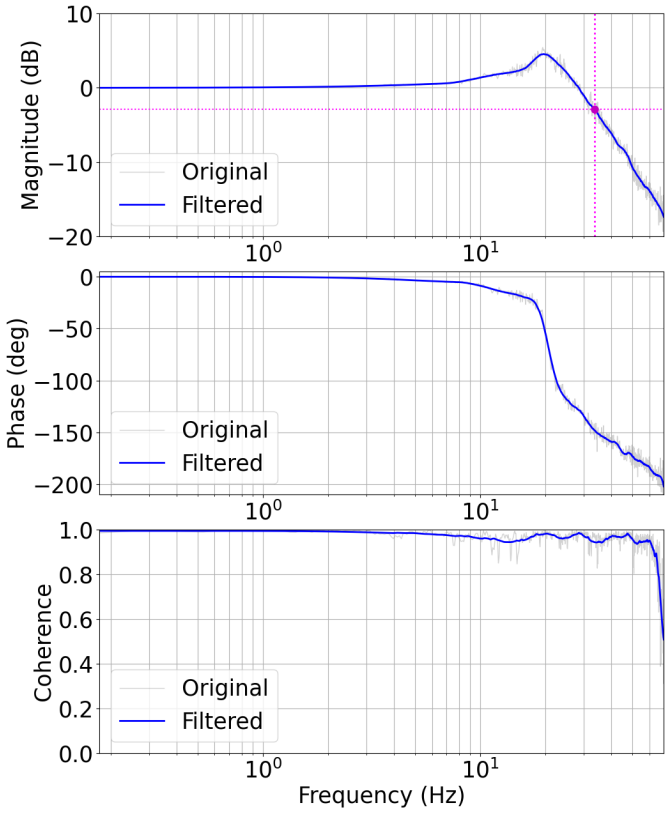

Fig. 14: *Bode plot comparing the original and filtered signals. The top two panels show the magnitude and the phase, while the bottom panel shows the coherence. The system exhibits a cutoff frequency of* $33.3\,Hz$*, a phase margin of* $46.1°$*, and a gain margin of* $13.2\,dB$*. The coherence remains above 0.9 up to 60 Hz.*

C. Admittance Control

Virtual inertia is a key component of admittance control and determines how the device responds to user-applied forces. Therefore, the feasible range of stable virtual inertia values was first identified before evaluating representative inertia settings in detail. Stable operation is observed between 8.0×10^{-5} and 4.0×10^{-4} kg m^2. Outside this range, tracking performance and controllability degrade.

At the lower bound (7.0×10^{-5} kg m^2), the system exhibits high sensitivity and oscillatory behavior, as shown in Figure 15. Small user inputs generate large accelerations and moment variations, resulting in oscillations of approximately $2°$. While the measured signals follow the target trajectory, controllability is reduced.

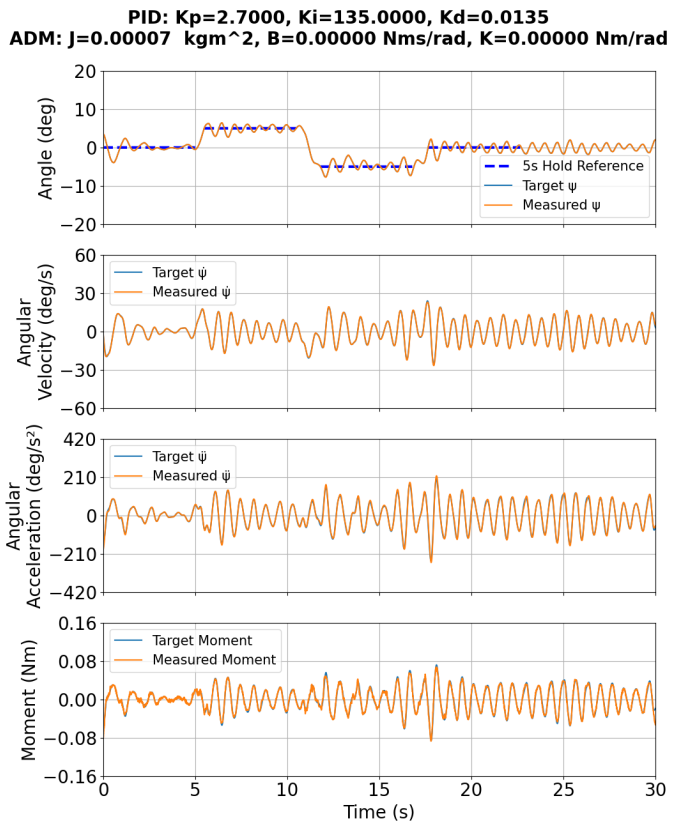

Fig. 15: *System response of the tracking task at a virtual inertia of* 7.0×10^{-5} *kg m*^{2}*, operating below the lower virtual inertia boundary and exhibiting pronounced oscillatory, sensitivity-driven behavior. The target angle corresponds to the admittance-computed angle, evaluated against the measured angle. Angular velocity and angular acceleration are obtained by differentiating the measured angle once and twice, respectively. The target moment is computed from the virtual inertia and the measured angle, while the measured moment reflects the real-time load-cell output.*

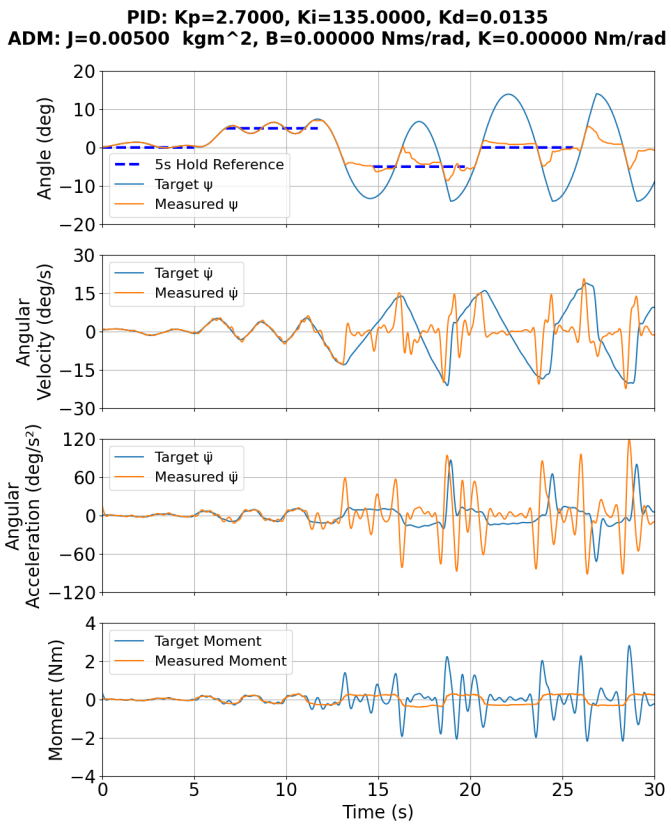

Fig. 16: *System response of the tracking task at a virtual moment of inertia of* 0.005 *kg m*^{2}*, operating above the upper virtual moment of inertia boundary and exhibiting reduced tracking performance with user input predominating the motion. The target angle corresponds to the admittance-computed angle, evaluated against the measured angle. Angular velocity and angular acceleration are obtained by differentiating the measured angle once and twice, respectively. The target moment is computed from the virtual inertia and the measured angle, while the measured moment reflects the real-time load-cell output.*

At the upper bound (0.005 kg m^2), the system exhibits slower dynamics, as shown in Figure 16. The target and measured angles align only briefly before diverging, indicating that user input dominates the rendered dynamics.

After identifying the feasible operating range, three representative inertia values were selected to evaluate the influence of virtual inertia on system behavior and rendering performance. These representative inertia values were selected: $J_{low} = 8.0 \times 10^{-5}$ kg m^2, $J_{mid} = 2.04 \times 10^{-3}$ kg m^2, and $J_{high} = 4.0 \times 10^{-3}$ kg m^2. The corresponding responses are shown in Figure 17.

At J_{low}, oscillations are present but reduced compared to the lower-bound case. At J_{mid}, oscillations decrease further, and the system becomes more stable during hold tasks. At J_{high}, tracking accuracy remains high, although small oscillations reappear. Across all conditions, the measured moment closely follows the target moment, indicating consistent enforcement of virtual dynamics.

While the previous figures provide a qualitative assessment of system behavior, quantitative metrics are required to compare performance across inertia conditions. Therefore, angle and moment RMSE values were calculated to evaluate tracking accuracy and virtual-dynamics rendering performance.

The angle RMSE results in Figure 18 show that tracking errors remain below $0.6°$ for all inertia values. At the lowest inertia, $J_{\min}$, the error is highest and most variable (median $0.57°$, IQR 0.53–$0.58°$, $\sigma = 0.091°$). Increasing the inertia to J_{mid} narrows the distribution (median $0.42°$, IQR 0.39–$0.42°$, $\sigma = 0.029°$). At $J_{\max}$, the median error remains low (median $0.41°$), though the spread increases again (IQR 0.35–$0.47°$, $\sigma = 0.078°$).

Beyond tracking accuracy, it is important to assess how closely the system follows the intended virtual dynamics. The moment RMSE values in Figure 19 increase with virtual inertia, reflecting the higher torque demands at larger inertia values. For $J_{\min}$, the moment error is small but moderately variable (median 0.0056 Nm, IQR 0.0041–0.0060 Nm, $\sigma = 0.0018$ Nm). At J_{mid}, the median error increases to 0.0081 Nm

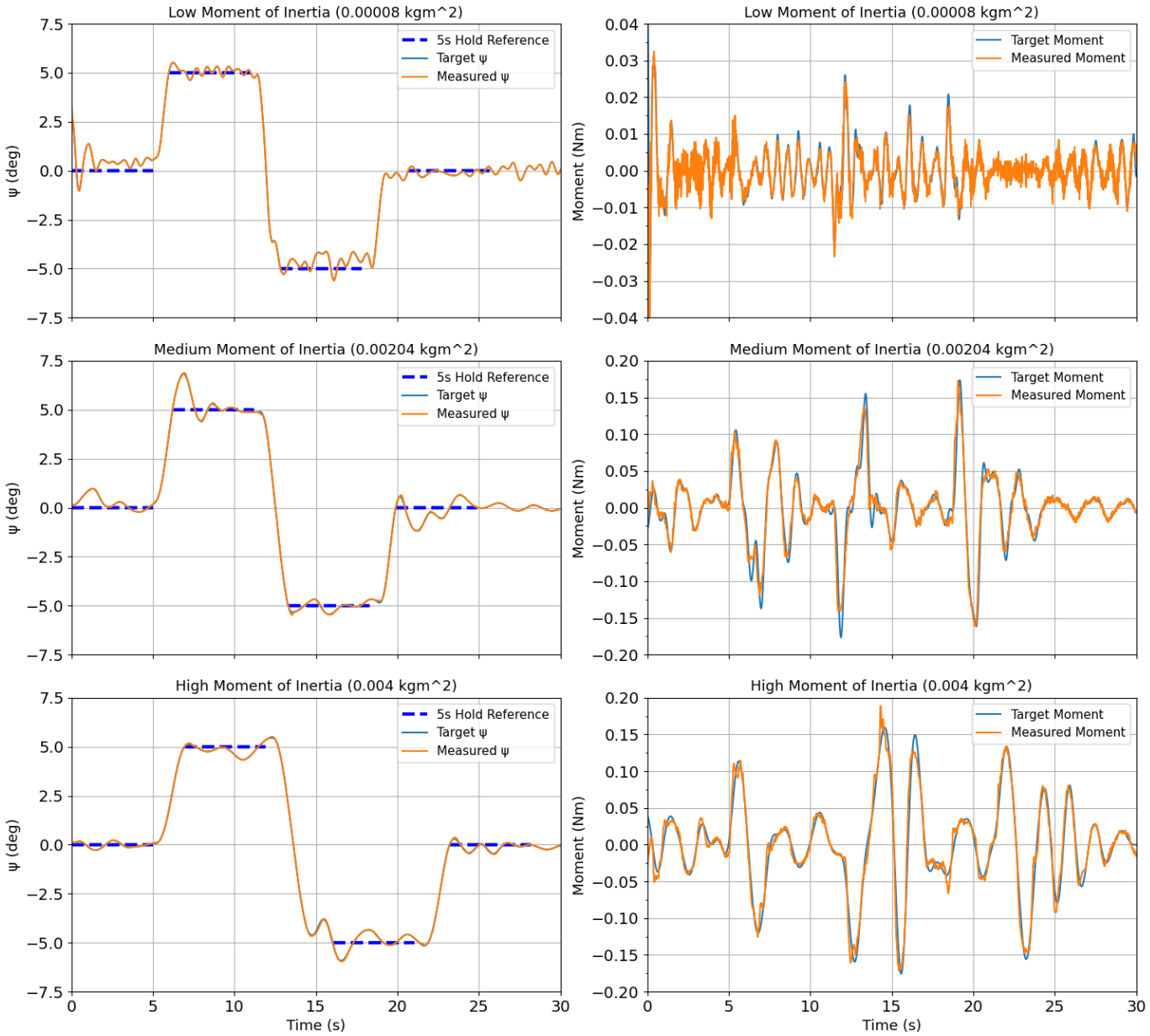

Fig. 17: *Comparison of system behavior under low, medium, and high virtual inertia settings during the tracking task. The target angle corresponds to the admittance-computed angle, evaluated against the measured angle. The target moment is obtained from the virtual inertia and the measured angle, while the measured moment reflects the real-time output of the load-cell.*

with a narrow distribution (IQR 0.0081–0.0083 Nm) and a similar standard deviation ($\sigma = 0.0018$ Nm). For $J_{\max}$, the moment RMSE increases further (median 0.014 Nm, IQR 0.013–0.014 Nm), while the variability decreases ($\sigma = 0.0006$ Nm).

Since the absolute moment RMSE naturally increases with virtual inertia, the errors were normalized by the applied inertia to better interpret their relative magnitude. The normalized results in Figure 20 show that $J_{\min} = 0.00008$ exhibits the largest relative error (median 29.3%, IQR 19.7%–30.9%, $\sigma = 10.9\%$). At $J_{\text{mid}} = 0.0020$, the normalized error decreases substantially (median 13.6%, IQR 13.4%–13.9%, $\sigma = 1.4\%$). For $J_{\max} = 0.004$, the normalized error increases slightly (median 14.5%, IQR 13.9%–14.7%, $\sigma = 1.30\%$), though it remains comparable to the mid-inertia condition.

D. Damping and Stiffness Effects

Besides inertia, admittance control relies on damping and stiffness to shape interaction dynamics. Therefore, the maximum achievable damping and stiffness values were evaluated using the medium-inertia condition as a baseline. Figure 21 shows these influences. The maximum stable values are identified as 0.01 Nms/rad for damping and 0.004 Nm/rad

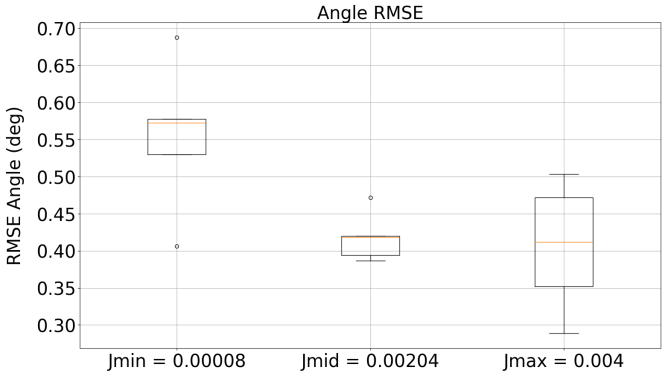

Fig. 18: *Box plot of the angle RMSE between the measured angle and the hold positions of the tracking task for different virtual-inertia values.*

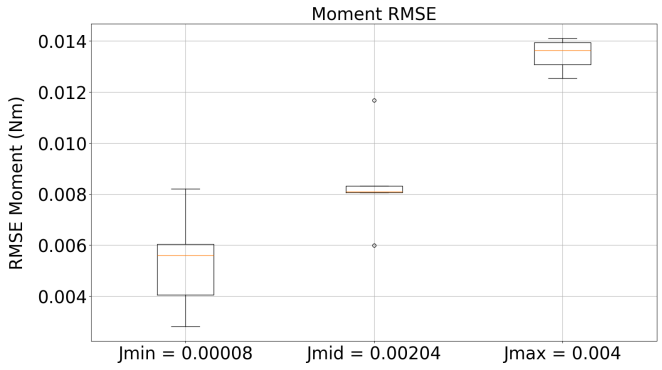

Fig. 19: *Box plot of the force RMSE between the measured angle and the target angle of the tracking tasks for different virtual inertia values.*

for stiffness. Increasing damping results in a slower but more stable response with reduced oscillations. Increasing stiffness increases interaction forces and leads to more pronounced oscillatory behavior. In the combined condition, system behavior is dominated by damping, indicating a stronger stabilizing effect compared to stiffness within the tested range.

V. Discussion

A. PID Controller Performance

Both PI and PID control strategies were evaluated to determine which configuration provided the most stable and responsive behavior for the hand module. The PI controller showed sustained oscillatory behavior after the step input, indicating insufficient damping and limited robustness during interaction with the user. In contrast, the PID controller significantly improved system stability by introducing derivative action, which reduced oscillations and improved settling behavior.

Although the PID controller achieved stable operation, the observed overshoot and underdamped response indicate that the system remained limited by PID tuning and actuator nonlinearities. The Ziegler and Nichols tuning method is known to be an aggressive tune. Additionally, the dead-zone behavior of the DC motor and the voltage drop introduced

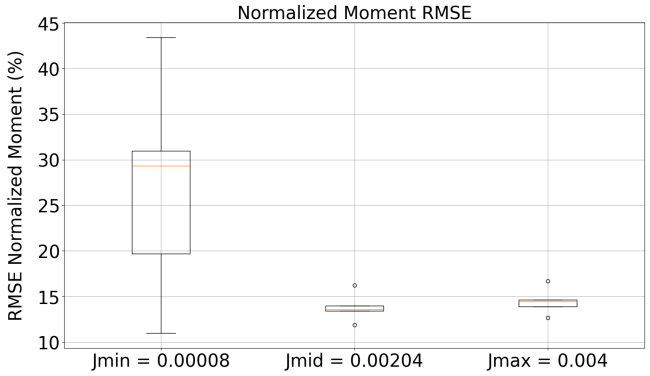

Fig. 20: *Box plot of the normalized force RMSE between the measured angle and the target angle of the tracking tasks for different virtual inertia values.*

by the L298N motor driver reduced the linearity of the actuator response. These nonlinear effects complicated precise low-force rendering and likely contributed to the remaining oscillatory behavior.

B. Mechanical Performance

The handle operated over the full designed range of motion of $\pm 15^{\circ}$. During the maximum virtual inertia test (Figure 16), a maximum torque of 0.32 Nm was measured, corresponding to 4.8 N. Both mechanical requirements were therefore achieved.

C. Feasibility of Admittance Control

The primary objective of this thesis was to determine whether admittance control could be implemented in an ultra-low-cost haptic device. The results demonstrate that this is feasible within a limited but practical operating range. The developed system successfully rendered virtual inertia, damping, and stiffness while maintaining stable human–robot interaction during the tracking tasks.

The admittance controller exhibited a stable virtual inertia range between 8.0×10^{-5} – 4.0×10^{-3} kg m^2. Within this range the plots show that the system perfomes the virtual dynamics. Furthermore, the controller successfully reproduced the expected qualitative effects of inertia, damping, and stiffness. Increasing inertia resulted in slower motion responses, increased damping reduced oscillations while requiring larger interaction forces, and increased stiffness introduced spring-like restoring behavior.

These findings indicate that the admittance controller operated according to the intended physical principles. The results therefore support the hypothesis that meaningful virtual dynamics can be rendered using highly affordable hardware components.

However, the achievable range of stable virtual dynamics was significantly constrained compared to high-end haptic systems such as the SEP. The low-cost implementation introduced several sensing, actuation, and computational limitations that directly affected controller performance.

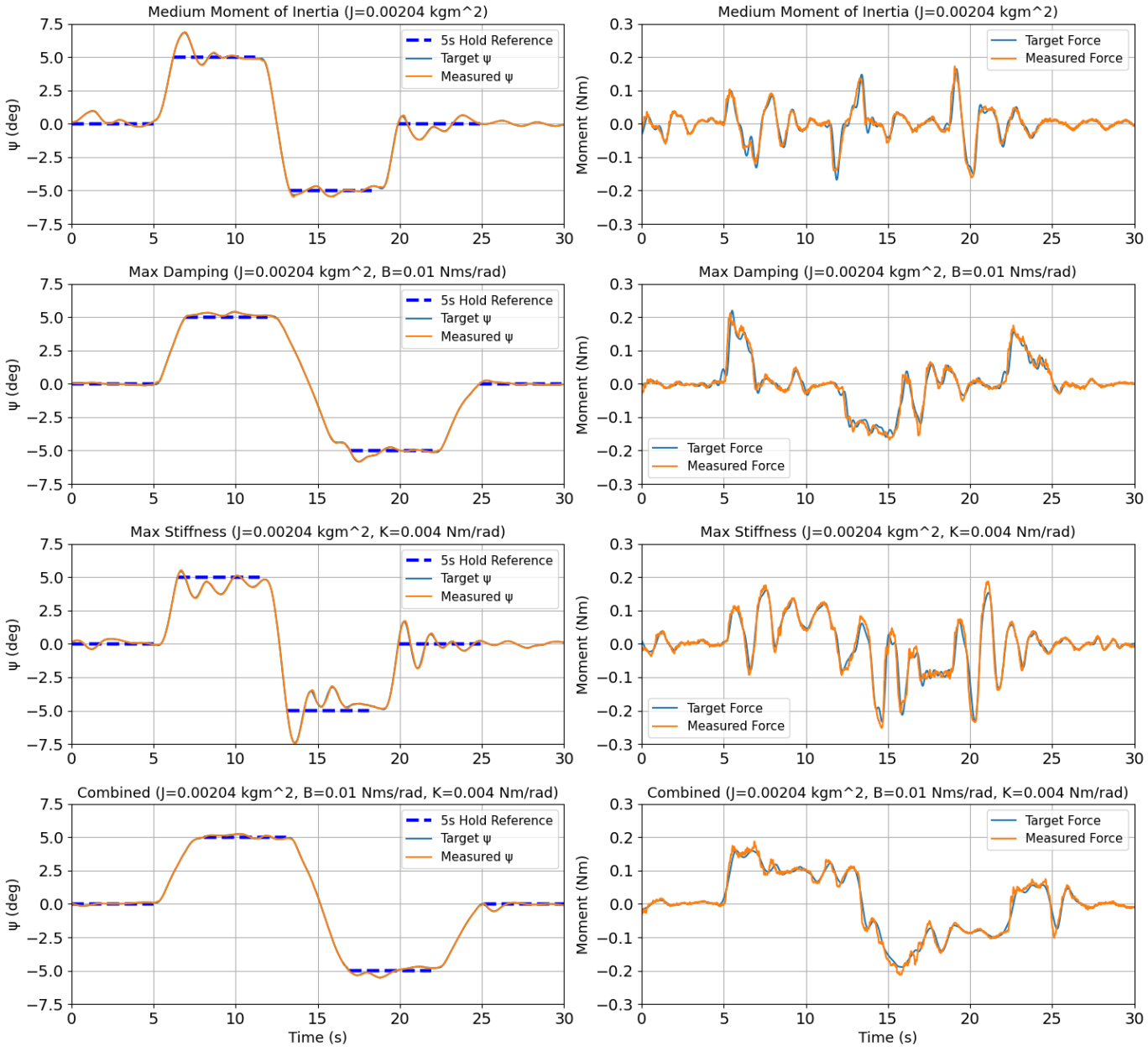

Fig. 21: *System response for different combinations of virtual damping and stiffness at medium inertia. The target angle corresponds to the admittance-computed angle, evaluated against the measured angle. The target moment is obtained from the virtual inertia and the measured angle, while the measured moment reflects the real-time output of the load-cell.*

D. Relevance for Neurological Assessment

The ability to render controllable virtual dynamics is particularly relevant for quantitative neurological assessment. Previous studies have used admittance-controlled environments to investigate how movement behavior changes under different mechanical conditions. The stable rendering of virtual inertia, damping, and stiffness demonstrated in this study suggests that similar experimental paradigms may be achievable using substantially lower-cost hardware.

Of particular interest is the demonstrated range of virtual inertia that could be rendered while maintaining stable interaction. Changes in virtual inertia directly influence the force requirements and movement strategies needed to perform a task. As a result, inertial environments may provide a means of probing motor adaptation and force regulation under controlled conditions. The ability to systematically vary these dynamics therefore represents a potentially valuable feature for future assessment applications.

Although the dynamic performance of the present system is more limited than that of dedicated rehabilitation robots, the results indicate that low-cost admittance-controlled devices may still be capable of generating meaningful variations in

interaction dynamics. This could facilitate future research into quantitative assessment approaches that would otherwise require more expensive robotic platforms.

E. Influence of Stroke-Related Impairments

The current evaluation was conducted with a healthy participant, whereas the intended users are individuals with neurological impairments whose interaction characteristics may differ substantially.

A key factor is reduced proprioception after stroke, which can limit the ability to accurately perceive limb position and movement [3]. Consequently, differences in virtual inertia that are clearly perceptible in healthy users may be less distinguishable in this population, motivating future work on perceptual sensitivity under impaired sensory conditions.

Stroke-related reductions in voluntary force and motor control may also constrain the usable range of virtual inertia, as higher values require greater interaction forces [2]. This suggests that controller adaptation may be necessary to match individual strength levels.

In addition, abnormal muscle co-contraction and pathological synergies may alter the effective mechanical impedance of the human–robot system, potentially affecting admittance controller stability. Since human-generated damping already influenced system behavior in this study, such changes could further impact the range of stable virtual dynamics.

Finally, because stroke synergies often involve coordinated multi-joint activation, extending the current SEP—which primarily targets shoulder and elbow motion—with hand sensing could improve the assessment of upper-limb impairment and provide deeper insight into synergy patterns.

F. Influence of Low-Cost Hardware on Admittance Control

The use of ultra-low-cost hardware strongly influenced the behavior and limitations of the admittance controller. Admittance control is inherently sensitive to sensor noise, force-measurement errors, and time delays because the measured interaction force directly determines the generated motion. As a result, limitations in sensing and control hardware had a direct impact on the rendered virtual dynamics.

One of the most important limitations originated from the force-sensing system. The HX711 amplifier restricted the effective force-measurement bandwidth to approximately 80 Hz and introduced quantization noise and low-frequency drift. These effects reduced the smoothness and accuracy of the measured force signal. Since the admittance controller converted this force directly into motion, noise in the force signal propagated into the virtual dynamics. This behavior became particularly visible at low virtual inertia values, where small force variations produced large accelerations and oscillatory behavior. Making the handle jitter, additionally, when trying to operate the controller with low inertia the user tends to lose their grip. Hence, decreasing the damping on which the PID relies.

The normalized moment RMSE was highest for the lowest inertia condition, indicating that force-measurement inaccuracies became increasingly dominant when the virtual inertia decreased. This demonstrates that low virtual inertia environments are particularly sensitive to force-sensor quality and controller bandwidth. The lower inertia boundary therefore appears to be primarily constrained by sensing noise and delay.

At high virtual inertia, performance was limited by actuator capability. The DC motor and L298N driver could not generate enough torque to resist user input. As a result, users could overpower the system and the handle no longer tracked the admittance reference accurately.

Additional limitations originated from the computational hardware. The Arduino Uno and serial communication introduced timing jitter and delays within the control loop. Although the controller operated at 1 kHz, the effective sensor and logging frequencies were substantially lower, particularly for the force sensor. These delays reduced the achievable stability margins and constrained the maximum renderable damping and stiffness.

Together, these observations demonstrate that the performance limitations of the system were directly related to the use of inexpensive hardware components. Nevertheless, despite these constraints, the system remained capable of rendering stable and distinguishable virtual dynamics over a meaningful operating range.

G. Trade-Off Between Cost and Performance

This work demonstrates the trade-off between affordability and haptic performance. The complete system cost remained below 50 euros by using consumer-grade actuators, sensors, and control electronics instead of industrial components.

Despite reduced performance, the device achieved stable admittance control within practical limits, indicating that low-cost haptic systems may be suitable for rehabilitation applications. However, the lower-cost hardware reduced sensing accuracy, actuator performance, and controller bandwidth, resulting in lower transparency, reduced stability at extreme parameter values, and greater sensitivity to user overpowering and measurement noise. Therefore, while feasible, the system does not yet match the performance of clinical-grade rehabilitation robots.

H. Limitations

Several limitations of the current system should be considered when interpreting the results. First, thermal effects in the DC motor lead to gradual misalignment between the encoder magnet and the sensing element during prolonged operation. This introduces measurement drift and reduces the accuracy and repeatability of the angle estimation over time, particularly in longer experimental sessions.

Second, the PID controller tuning is based on the Ziegler–Nichols method, which typically yields relatively aggressive gain settings. While this enables fast transient response, it also increases sensitivity to measurement noise and can reduce robustness, especially under low-inertia and highly interactive conditions. More systematic or application-specific tuning approaches could potentially improve stability margins and expand the usable range of virtual dynamics.

Third, the actuator and motor driver represent a major performance bottleneck. The low-cost DC motor provides limited torque and exhibits cogging and dead-zone effects, while the L298N driver introduces significant voltage drops that further reduce effective actuation capability. The system can be overpowered by the user at higher virtual inertia settings, limiting virtual dynamics.

Fourth, the sensing system imposes bandwidth and signal quality constraints. The load cell amplifier (HX711) limits the effective force sampling rate to approximately 80 Hz and introduces quantization noise, drift, and jitter. These effects propagate directly into the admittance controller, since force measurements are mapped into motion generation, thereby reducing smoothness and stability of the rendered interaction. Although the microcontroller is capable of kHz-level control execution, the overall closed-loop performance is primarily constrained by sensor bandwidth and communication latency.

Fifth, the system is sensitive to measurement noise and limited signal conditioning. Force and position signals are affected by sensor noise and drift, which can degrade the accuracy of the computed virtual dynamics. While basic filtering is implemented, higher-quality sensing hardware could improve signal accuracy.

Finally, controller performance is partly dependent on human interaction dynamics. The stability of the system is influenced by the damping introduced by the participant's grip and movement behavior, meaning that performance may vary between users and experimental conditions. This reduces the consistency of the controller tuning across different interaction styles and limits full generalizability.

I. Future Work

Future work should focus on improving the robustness and clinical applicability of the system. More refined PID tuning methods could be investigated to improve controller performance and expand the range of stable virtual dynamics.

The mechanical design could also be improved to reduce the influence of motor heating on encoder alignment during prolonged operation. Improving thermal management or redesigning the encoder mounting may increase measurement stability and repeatability.

In addition, future versions of the device could benefit from improved actuation and sensing hardware. A stronger motor would increase the available torque and may be particularly important when evaluating stroke patients, who often exert larger interaction forces and experience greater difficulty with delicate movements. Likewise, higher-quality sensors could improve measurement reliability by reducing noise, latency, and drift.

Finally, the system should be evaluated with stroke survivors to determine whether the rendered virtual dynamics are sufficiently perceptible and useful for quantitative neurological assessment.

VI. Conclusion

This thesis investigated the feasibility of implementing admittance control in an ultra-low-cost haptic device. The developed hand module successfully rendered virtual inertia, damping, and stiffness while maintaining stable human–robot interaction within a practical operating range. The complete system was realized using widely available components with a total hardware cost below 50 euros.

The results demonstrate that admittance control is feasible using low-cost hardware, although system performance is strongly constrained by sensing bandwidth, actuator limitations, measurement noise, and computational delays. These limitations reduced the achievable range and accuracy of the rendered virtual dynamics compared to high-end rehabilitation systems.

Nevertheless, the presented system demonstrates that meaningful admittance-controlled interaction can be achieved using highly affordable hardware platforms. This suggests that low-cost haptic devices may provide accessible alternatives future low-resource rehabilitation technologies.

References

[1] V. L. Feigin, M. Brainin, B. Norrving, S. O. Martins, J. Pandian, P. Lindsay, M. F Grupper, and I. Rautalin, "World Stroke Organization: Global Stroke Fact Sheet 2025," *International Journal of Stroke*, vol. 20, no. 2, pp. 132–144, Feb. 2025. [Online]. Available: https://pmc.ncbi.nlm.nih.gov/articles/PMC11786524/

[2] P. Raghavan, "Upper Limb Motor Impairment Post Stroke," *Physical medicine and rehabilitation clinics of North America*, vol. 26, no. 4, pp. 599–610, Nov. 2015. [Online]. Available: https://pmc.ncbi.nlm.nih.gov/articles/PMC4844548/

[3] S. Doyle, S. Bennett, S. E. Fasoli, and K. T. McKenna, "Interventions for sensory impairment in the upper limb after stroke," *The Cochrane Database of Systematic Reviews*, vol. 2010, no. 6, p. CD006331, Jun. 2010. [Online]. Available: https://www.ncbi.nlm.nih.gov/pmc/articles/PMC6464855/

[4] E. Ekstrand, L. Rylander, J. Lexell, and C. Brogårdh, "Perceived ability to perform daily hand activities after stroke and associated factors: a cross-sectional study," *BMC Neurology*, vol. 16, p. 208, Nov. 2016. [Online]. Available: https://www.ncbi.nlm.nih.gov/pmc/articles/PMC5093923/

[5] L. L. van der Velden, B. Onneweer, C. J. W. Haarman, J. L. Benner, M. E. Roebroeck, G. M. Ribbers, and R. W. Selles, "Development of a single device to quantify motor impairments of the elbow: proof of concept," *Journal of NeuroEngineering and Rehabilitation*, vol. 19, no. 1, p. 77, Jul. 2022. [Online]. Available: https://doi.org/10.1186/s12984-022-01050-2

[6] H. J. van der Krogt, C. G. Meskers, J. H. de Groot, A. Klomp, and A. Et., "The gap between clinical gaze and systematic assessment of movement disorders after stroke," *Journal of NeuroEngineering and Rehabilitation*, 2012. [Online]. Available: https://sci-hub.su/10.1186/1743-0003-9-61

[7] H. van der Krogt, A. Klomp, J. H. de Groot, E. de Vlugt, F. C. van der Helm, C. G. Meskers, and J. H. Arendzen, "Comprehensive neuromechanical assessment in stroke patients: reliability and responsiveness of a protocol to measure neural and non-neural wrist properties," *Journal of NeuroEngineering and Rehabilitation*, vol. 12, no. 1, p. 28, Mar. 2015. [Online]. Available: https://doi.org/10.1186/s12984-015-0021-9

[8] Starsky, Sangani, McGuire, Logan, and A. Et., "Reliability of Biomechanical Spasticity Measurements at the Elbow of People Poststroke," *Archives of Physical Medicine and Rehabilitation*, 2005. [Online]. Available: https://sci-hub.st/https://www.sciencedirect.com/science/article/abs/pii/S0003999305003217

[9] Sloot, van der Krogt, Groep, van Eesbeek, and A. Et., "The validity and reliability of modelled neural and tissue properties of the ankle muscles in children with cerebral palsy," *Gait & Posture*, 2015. [Online]. Available: https://sci-hub.st/https://www.sciencedirect.com/science/article/abs/pii/S0966636215004476
[10] Trumbower, Ravichandran, Krutky, and Perreault, "Contributions of Altered Stretch Reflex Coordination to Arm Impairments Following Stroke," *Journal of Neurophysiology*, 2010. [Online]. Available: https://sci-hub.st/https://journals.physiology.org/doi/full/10.1152/jn.00804.2009
[11] M. D. Ellis, Y. Lan, J. Yao, and J. P. A. Dewald, "Robotic quantification of upper extremity loss of independent joint control or flexion synergy in individuals with hemiparetic stroke: a review of paradigms addressing the effects of shoulder abduction loading," *Journal of NeuroEngineering and Rehabilitation*, vol. 13, no. 1, p. 95, Oct. 2016. [Online]. Available: https://doi.org/10.1186/s12984-016-0203-0
[12] McPherson, Stienen, Schmit, and Dewald, "Biomechanical parameters of the elbow stretch reflex in chronic hemiparetic stroke," *Experimental Brain Research*, 2018. [Online]. Available: https://sci-hub.st/https://link.springer.com/article/10.1007/s00221-018-5389-x
[13] J. C. van Zanten, K. ter Welle, C. J. Haarman, A. C. Schouten, M. van de Ruit, W. Mugge, and A. H. Stienen, "System Performance Analysis of the Shoulder Elbow Perturbator," in *2025 International Conference On Rehabilitation Robotics (ICORR)*, May 2025, pp. 346–351. [Online]. Available: https://ieeexplore.ieee.org/abstract/document/11063005
[14] A. L. Neil, "Corrigendum to: Out-of-pocket payments: impacts on healthcare decision-making and system and individual level measures to minimise the burden," *Australian Health Review*, vol. 47, no. 4, p. 518, Aug. 2023. [Online]. Available: https://doi.org/10.1071/AH22244_CO
[15] J. M. Blennerhassett, L. M. Carey, and T. A. Matyas, "Grip force regulation during pinch grip lifts under somatosensory guidance: comparison between people with stroke and healthy controls," *Archives of Physical Medicine and Rehabilitation*, vol. 87, no. 3, pp. 418–429, Mar. 2006.
[16] R. S. Johansson and G. Westling, "Coordinated isometric muscle commands adequately and erroneously programmed for the weight during lifting task with precision grip," *Experimental Brain Research*, 1988. [Online]. Available: https://sci-hub.su/10.1007/bf00247522
[17] J. R. Flanagan and A. Wing, "The stability of precision grip forces during cyclic arm movements with a hand-held load," *Experimental Brain Research*, 1990. [Online]. Available: https://sci-hub.su/10.1007/bf00233045
[18] T. Flash and N. Hogan, "The coordination of arm movements: an experimentally confirmed mathematical model," *The Journal of Neuroscience*, 1985. [Online]. Available: https://sci-hub.su/10.1523/jneurosci.05-07-01688.1985
[19] M. J. Puerto, E. Sanchez, and J. J. Gil, "Control strategies applied to kinesthetic haptic devices," *2009 IEEE Workshop on Robotic Intelligence in Informationally Structured Space*, 2009. [Online]. Available: https://sci-hub.box/https://ieeexplore.ieee.org/abstract/document/4937918
[20] A. Q. Keemink, H. van der Kooij, and A. H. Stienen, "Admittance control for physical human–robot interaction," *The International Journal of Robotics Research*, vol. 37, no. 11, pp. 1421–1444, Sep. 2018. [Online]. Available: https://doi.org/10.1177/0278364918768950
[21] O. Martinez, Nunez, Liao, Morimoto, and A. Et., "Evolution and Analysis of Hapkit: An Open-Source Haptic Device for Educational Applications," *IEEE Transactions on Haptics*, 2020. [Online]. Available: https://sci-hub.st/https://ieeexplore.ieee.org/abstract/document/8878113
[22] "Hapkit." [Online]. Available: https://hapkit.stanford.edu/index.html
[23] Gassert, Metzger, Leuenberger, Popp, and A. Et., "Physical Student–Robot Interaction With the ETHZ Haptic Paddle," *IEEE Transactions on Education*, 2013. [Online]. Available: https://sci-hub.st/10.1109/te.2012.2219310
[24] "0.78 Kg Micro Load Cell." [Online]. Available: https://eu.robotshop.com/products/micro-load-cell-0-78-kg
[25] K. J. Åström and R. M. Murray, "Feedback Systems - An Introduction for Scientists and Engineers," vol. Second Edition, Jul. 2020.

VII. Appendix

A. Drum geometry

As shown in Figure 22, if only α were considered, the capstan would move directly to the edge of the drum during operation. To prevent the capstan from surpassing the edge, an additional angular margin β is introduced, effectively increasing the width of the drum. Substituting the previously determined parameters into Equation 14 yields $\beta = 3.3°$. This margin provides a safety buffer on both sides of the drum to ensure reliable contact throughout the motion range. So the total angle of the drum is 33.2°.

$$\beta = \arctan \frac{r_c}{r_d + r_c} \tag{14}$$

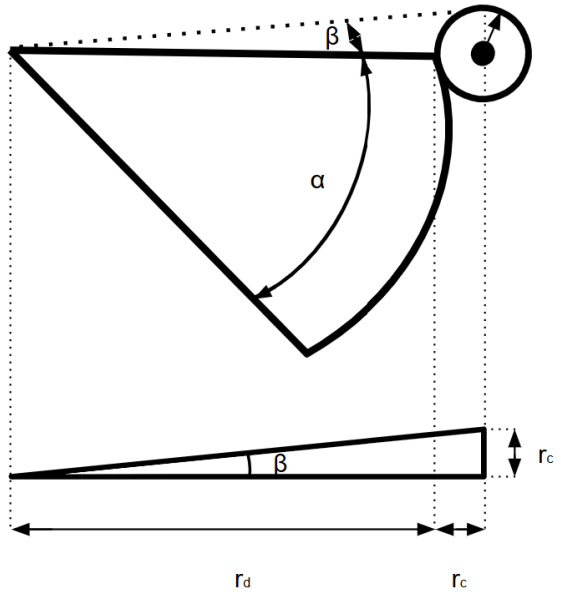

Fig. 22: *Geometric diagram showing the angular relationship and key dimensions between the Hapkit drum and the capstan. The angle α represents the base angle of the drum, while β denotes the additional safety margin, which can be determined by the drum radius r_d and the capstan radius r_c. The combination of these angles defines the total angle of the drum.*